Multiple absorption regimes in simple lithography-free structures leading to ultrathin slabs

Carlos Lezaun [1], David Navajas [1], Iñigo Liberal [1,2] and Miguel Beruete [1,2,*]
[1] *Antennas Group-TERALAB, Electric and Electronic Engineering Department, Public University of Navarra, Campus Arrosadía, 31006 Pamplona, Spain*
[2] *Institute of Smart Cities, Universidad Pública de Navarra, 31006 Pamplona, Spain*

(Received 8 March 2024; accepted 5 June 2024; published 8 July 2024)

Electromagnetic absorbers serve as fundamental components for a wide range of applications, encompassing energy and heat management, sensing, and communications. In this study, we explore several complex permittivity combinations for lithography-free material-reflector and material-spacer-reflector configurations that lead to perfect absorption peaks across distinct permittivity regimes and varying thicknesses. We provide an extensive analysis of angle and polarization dependencies, specifically using silicon carbide as an illustrative example. Our findings reveal the potential for harnessing different absorption regimes within a single device, thus enabling the realization of multiband absorption capabilities. Furthermore, we demonstrate perfect absorption linked with extreme values of permittivity, and we find the conditions to get perfect absorption in ultrathin slabs. In addition, we carry out an analysis about the response at oblique incidence, and we identify a particular mode in the negative permittivity region and its hybridization with epsilon-near-zero modes at oblique incidence. This investigation serves as a valuable standardization of absorber design, offering insights to develop perfect absorbers for infrared applications such as thermal emission, communications, and sensing.

DOI: 10.1103/PhysRevB.110.045408

I. INTRODUCTION

The emission and absorption of infrared light plays a pivotal role in numerous technologies, including thermophotovoltaics [1,2], radiative cooling [3,4], bioengineering [5,6], sensing [7,8], optoelectronics [9–11], thermal camouflaging [12,13], and thermal management [14–16], among others. To harness the full potential of these technologies, there is a growing need to dynamically modulate the absorption response within compact and scalable devices. However, the performance of such small devices is often hindered by the limited interaction between light and matter.

This emission or absorption spectrum (in thermal equilibrium both are identical) can be engineered by means of resonators based on either cavities or photonic periodic structures [17–19]. A classical solution is the Salisbury screen, which has evolved into more intricate multilayer devices [20]. Advanced versatility can be achieved by means of photonic periodic structures based on metamaterials [21]. However, their complex manufacturing processes and the necessity for extremely small features at high frequencies have hindered widespread adoption. As an alternative, one-dimensional multilayer structures are gaining popularity due to their simplicity, cost-effectiveness, and scalability, even though they offer somewhat limited control over light [22].

In the realm of ultrathin structures, the absorption limit has been pushed to its boundaries through the utilization of epsilon-near-zero media (ENZ) [23]. Among its properties, ENZ media present high light-matter interaction, allowing to reduce the device dimensions [24,25]. Notably, a thin perfect absorber composed of three layers of VO_2, aluminum-doped zinc oxide (AZO) and ZnO, with a combined thickness of only several hundred nanometers was demonstrated recently [26]. Furthermore, dynamic emission controlled by temperature variations can be achieved by means of phase-change materials [27]. In an alternative approach, a metal layer on top of a silicon carbide (SiC) substrate operating at the ENZ regime has been proposed as a high impedance surface for ultrathin absorbers [28] with high angular stability [29]. Even particle resonances have been exploited to absorb within atomically thin two-dimensional (2D) materials [30,31], again with seemingly complex manufacturing.

Despite all this previous work, there is still a gap in the development of a comprehensive approach for designing monolayer and bilayer absorbers atop a reflector. While a significant amount of progress has been made to explain the critical coupling condition for achieving perfect absorbers [32], and monolayer ENZ media have already been studied [33], no work to date has effectively integrated all the requisite characteristics to attain perfect absorption in a broad range of scenarios. This work covers this gap by presenting a thorough analysis based on transmission line theory [34] of various configurations involving single and bilayer structures to achieve absorption peaks. We specifically focus on two straightforward scenarios: a slab placed on a reflector and a slab separated from the reflector by a dielectric layer. These scenarios were chosen for their simplicity, as they avoid photolithography and complex multilayer structures. In Sec. II, we begin by examining a single layer of an arbitrary material atop a reflective surface. We explore all feasible combinations of the material's complex permittivity and thickness that result

*Contact author: miguel.beruete@unavarra.es

 ©2024 American Physical Society

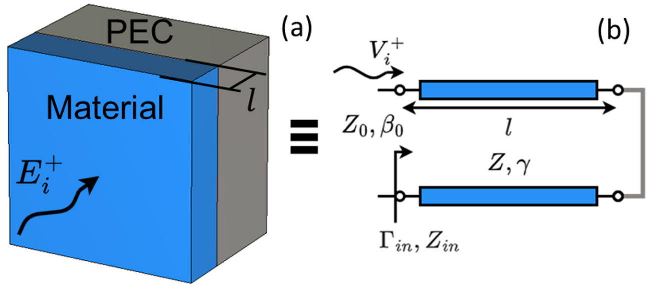

FIG. 1. (a) Structure of a generic nonmagnetic and nondispersive material on top of a PEC with (b) its equivalent circuit.

in absorption peaks while providing an in-depth understanding of the underlying physical principles. Furthermore, we identify several cases of interest in which absorption peaks can be obtained using ultrathin structures at both normal and oblique incidence. Then, we extend our analysis by introducing a dielectric spacer between the material and the reflector. To move closer to practical implementation, in Sec. III we replace the arbitrary material with silicon carbide (SiC) in both configurations. This enables us to validate our predictions and explore the effects of incidence angle and polarization across different permittivity regimes. Our results are consistent with existing research on Salisbury screens and ENZ media, and they also expand upon this knowledge by demonstrating that incorporating SiC as the resistive layer enables the integration of both absorption modes. We also prove that low impedance materials attain perfect absorption, and we emphasize the importance of the dispersion of the layers to obtain multiband operation within simple structures. This work contributes to a deeper understanding of monolayer and bilayer absorbers on top of reflectors, holding potential relevance for applications in thermal emission as well as communication and sensing.

II. THEORETICAL ANALYSIS

A. Generic lossy material slab terminated in a reflector

Figure 1 depicts schematically the problem under consideration. It consists in a generic lossy material slab of thickness l laying on a perfect electric conductor (PEC) sheet and facing air on the other side. Such material is nonmagnetic ($\mu = 1$), and its electromagnetic response is fully characterized by a complex relative permittivity $\varepsilon = \varepsilon' - j\varepsilon''$ (note that in our analysis, we consider a time dependence in the form of $e^{j\omega t}$). Assuming plane-wave excitation from the air side, the structure can be analyzed by an equivalent transmission line (TL) terminated in a short circuit, as depicted schematically in Fig. 1(b) and described in [34]. Following this formalism, the generic material slab is modeled as a TL section of length l, normalized complex characteristic impedance $\overline{Z}$, and complex propagation constant γ:

$$\overline{Z} = 1/\sqrt{\varepsilon} = R + jX, \tag{1}$$

$$\gamma = jk_0\sqrt{\varepsilon} = \alpha + j\beta, \tag{2}$$

where $\overline{Z}$ stands for the impedance normalized to the air ($Z_0 = \sqrt{\mu_0/\epsilon_0}$), R and X are the resistance and reactance values of the normalized characteristic impedance, k_0 is the wave number in air, α is the attenuation constant, and β is the propagation constant inside the slab.

Applying the typical TL formalism [34], the normalized input impedance ($\overline{Z_{\text{in}}}$) and input reflection coefficient (Γ_{in}) can be calculated as

$$\overline{Z_{\text{in}}} = \overline{Z}\tanh(\gamma l) = \overline{Z}\tanh(\Phi), \tag{3}$$

$$\Gamma_{\text{in}} = \frac{\overline{Z_{\text{in}}} - 1}{\overline{Z_{\text{in}}} + 1}, \tag{4}$$

where $\Phi = \gamma l$, and we have implicitly assumed that $Z_L = 0\ \Omega$, as corresponds to a PEC sheet. The presence of a PEC at the load prohibits any transmission through the structure, and therefore any nonreflected power will be absorbed in the material, which is the only source of losses in this setup. Hence, the absorbance of the material can be directly calculated from the input reflection coefficient as $A = 1 - |\Gamma_{\text{in}}|^2$. From this expression, unity absorbance occurs if the input reflection coefficient vanishes ($\Gamma_{\text{in}} = 0$).

Inserting this condition in Eq. (4), it is found that perfect impedance matching at the input, $\overline{Z_{\text{in}}} = 1$, is necessary to get perfect absorption [32]. From Eq. (3), this happens when

$$\overline{Z} = \coth(\Phi). \tag{5}$$

To investigate the conditions under which absorption peaks appear, we conducted a thorough analytical study by mapping the absorbance as a function of ε' and ε'', with ε' varying from -5 to 15 and ε'' from 0 to 5 for different values of l/λ ranging from 0.1 to 2. A variety of absorption peaks were observed in all cases, including ultrathin substrates, which will be addressed in subsequent sections. To observe in detail the evolution of these peaks (marked with black asterisks) as the thickness increases, Figs. 2(a)–2(c) display the resulting color maps for three different cases with moderate thickness, $l/\lambda = 0.5$, 1, and 1.5. The use of relatively thick substrates is intentional, as they enable clear distinction between different permittivity regions.

As observed in the figure, all panels exhibit similar qualitative behavior. To provide a more in-depth analysis, we will focus on the case depicted in Fig. 2(c), corresponding to $l/\lambda = 1.5$. The absorption peaks (asterisks) coincide with the points where $\overline{Z_{\text{in}}} = 1$, as can be seen by comparing Fig. 2(c) with Figs. 3(a) and 3(b), which show the magnitude and phase of $\overline{Z_{\text{in}}}$ (white and black asterisks). The appearance of these absorption peaks can be explained by examining the behavior of $\overline{Z}$, as depicted in Figs. 3(c) and 3(d), and $\coth(\Phi)$, as illustrated in Figs. 3(e) and 3(f). As ε' approaches 0, the magnitude of $\overline{Z}$ tends to infinity, exhibiting a rapid initial decay before eventually converging asymptotically to 0 for larger permittivity values. Figure 3(d) shows that when $\varepsilon' > 0$, the phase of $\overline{Z}$ is less than 45°, indicating that the real part (Re{Z}) of the impedance predominates over the imaginary part (Im{Z}). Conversely when $\varepsilon' < 0$ the phase exceeds 45°, indicating that Re{Z} < Im{Z}. In turn, for $\varepsilon' > 0$ the magnitude of $\coth(\Phi)$ exhibits oscillations between 0 and ∞ while the phase varies between $-90°$ and 90°. This oscillating pattern plays a crucial role in achieving perfect impedance matching and hence absorption since it ensures the existence of a value where the function matches $\overline{Z}$, as demonstrated by comparing

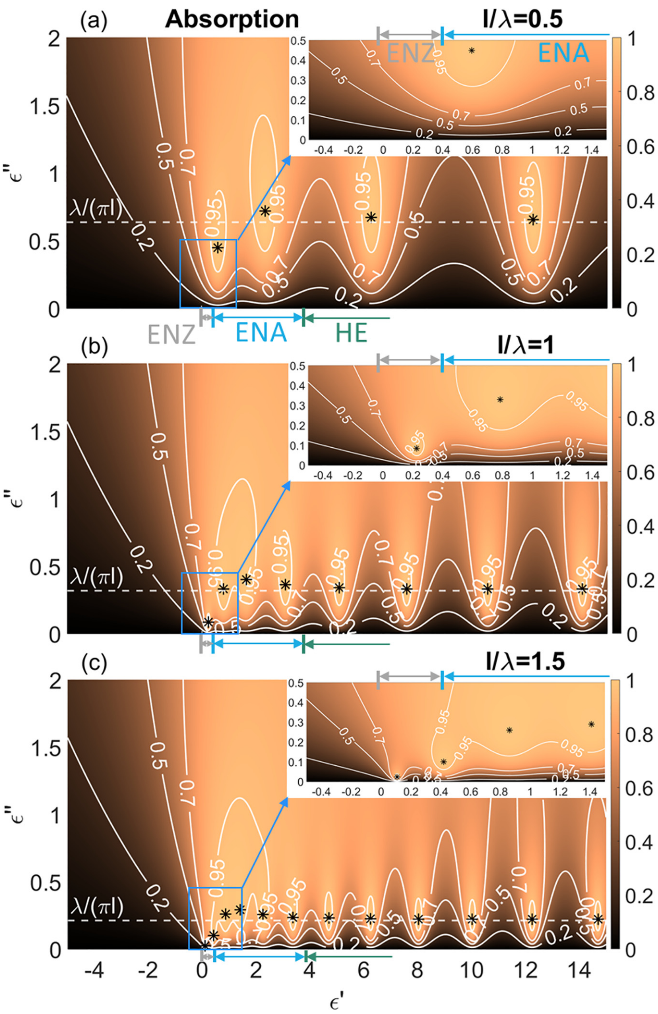

FIG. 2. Absorption color maps of the structure, with ε' and ε'' as variables, at various values of l/λ: (a) $l/\lambda = 0.5$, (b) $l/\lambda = 1$, and (c) $l/\lambda = 1.5$. Three distinct regions are identified and labeled as epsilon-near-zero (ENZ, $0 < \varepsilon' < 0.4$), epsilon-near-air (ENA, $0.4 < \varepsilon' < 4$), and high epsilon (HE, $\varepsilon' > 4$) areas. Inset images provide a closer examination of the ENZ and ENA regions, with asterisks denoting points of perfect absorption. Additionally, selected isoabsorption curves are highlighted by white lines and the asymptotic value of ε'' [see Eq. (6)] is marked with a dashed line.

Figs. 3(c) and 3(d) with Figs. 3(e) and 3(f), thereby satisfying Eq. (5). The previous discussion implies a complex material impedance with a relatively small imaginary part, high enough to ensure high absorption peaks but low enough to fulfill the matching condition.

Figures 3(e) and 3(f) demonstrate that the occurrence of unbounded oscillatory behavior is limited to positive values of ε'. When ε' is negative, then $\coth(\Phi) \approx 1$, and, as indicated above, $\overline{Z}$ is predominantly imaginary. This explains the absence of absorption peaks in this case because Eq. (5) can never be fulfilled. Intuitively, this implies that a material with a metal-like behavior ($\varepsilon' < 0$) can never give rise to absorption peaks in this setup.

Next, we are going to analyze in detail the different regions marked in Figs. 2 and 3, starting with the so-called epsilon-near-zero (ENZ) region, defined arbitrarily in this work as $0 < \varepsilon' < 0.4$. The first feature observed is the lack of absorption peaks for small values of l, as demonstrated in the inset of Fig. 2(a). Later we will demonstrate that this fact only holds true for normal incidence. For now, this can be explained by considering that small values of ε' correspond to small values of γ, as indicated by Eq. (2), and hence both the attenuation and propagation constants are small. Therefore, attaining significant absorption with a small attenuation constant requires a minimum thickness. In addition, the exceptionally narrow width of the first peak observed in the ENZ region [35], presented in more detail in the inset of Fig. 2(c), can be attributed to the rapid and pronounced variation of the impedance within that specific region. When $0 < \varepsilon < 1$, the impedance experiences a drastic change from infinity to 1. The perfect matching condition occurs for specific singular values, and even a slight variation in ε' leads to a rapid variation of the matching condition. As a result, the peak quickly disappears.

The next region under study is labeled epsilon-near-air (ENA), and it is situated (also arbitrarily) within the range $0.4 < \varepsilon' < 4$. This range is selected because the absorption peaks exhibit minimal differentiation, in stark contrast to the ultranarrow peaks obtained in the ENZ region. This can primarily be attributed to the absence of absorption decay between the peaks, as clearly observed around $\varepsilon' \approx 1$ in the inset picture of Figs. 2(b) and 2(c). In this region, the impedance variation is relatively small, and hence the matching condition depends primarily on the oscillations of $\coth(\Phi)$. However, the magnitude and phase variations between adjacent peaks are not significant enough to create a substantial mismatch between those points of perfect absorption within this range [see Figs. 3(e) and 3(f)]. Consequently, these peaks cannot be distinctly differentiated across the range of ε.

Finally, we examine the high epsilon region (HE) defined by $\varepsilon' > 4$, where the lobes are moderately narrow and well distinguishable, as seen in the right part of Figs. 2(a)–2(c). The separation of the lobes is now primarily attributed to a slower oscillation of $\coth(\Phi)$ with higher magnitude and phase variation between matching points [see Figs. 3(e) and 3(f)], leading to a pronounced mismatch between consecutive matching points. Additionally, according to Eq. (2), as the value of ε increases, so does the attenuation constant and losses of the medium. As a consequence, perfect absorption solutions can emerge with sufficiently high permittivity values, for arbitrarily small thickness (see Sec. II B). Moreover, the distance between adjacent peaks is larger in the HE region in Figs. 2(a)–2(c). For low ε'', $\coth(\Phi) \approx \cot(\Phi)$, where the latter function has a periodicity of $\Phi = n\pi, n \in \mathbb{N}$ and by Eq. (2), $\Phi \propto \sqrt{\varepsilon} l$. Therefore, the periodicity seen in Figs. 3(e)–3(f) has a quadratic relation with ε' and a linear relation with the thickness l. Hence, as ε' increases, the distance between absorption peaks also increases, and vice versa. A notable result observed in the plots is the occurrence of peaks for ε'' values that tend asymptotically to $\lambda/\pi l$ as ε' increases. A detailed derivation of this result is presented in [36], SI.A, underscoring its significant consequences. This phenomenon suggests that absorption peaks are achieved even with a slab of infinitesimal thickness, as detailed in the following section.

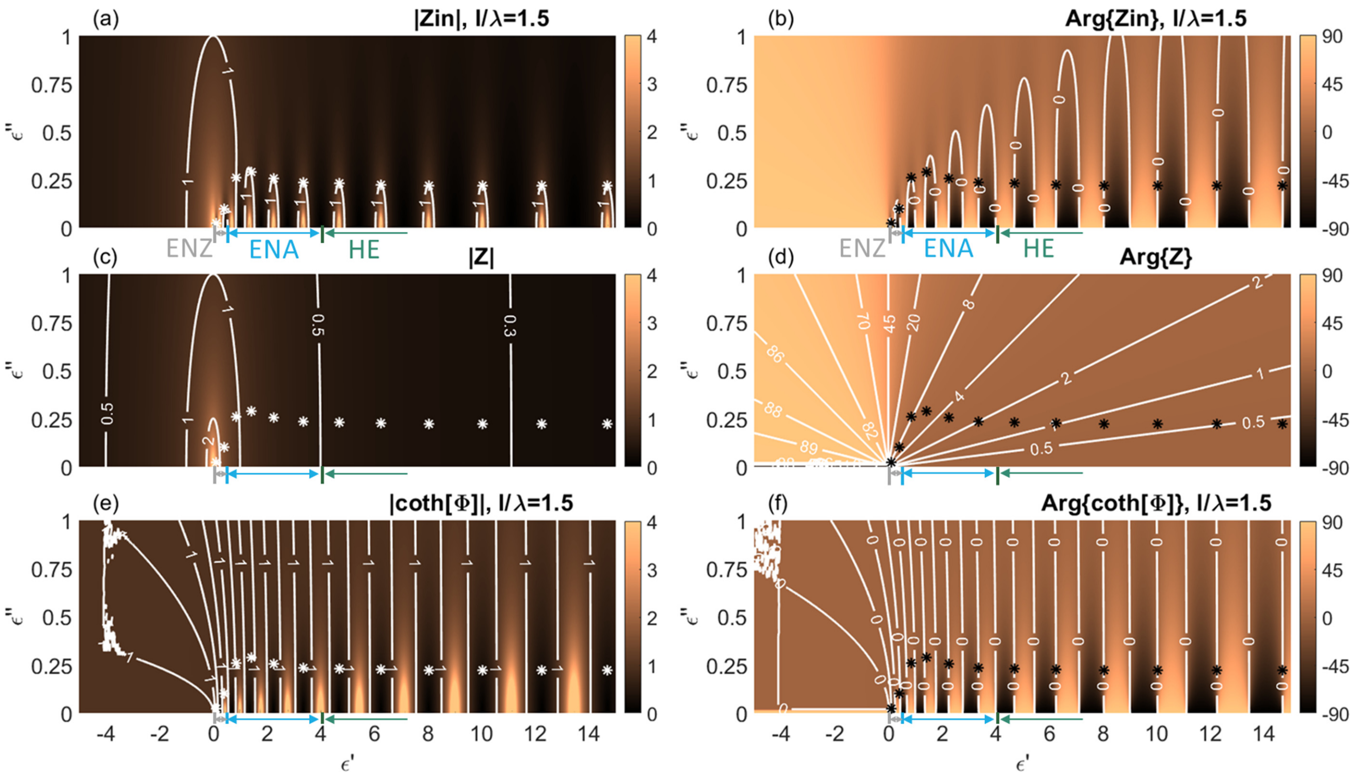

FIG. 3. Magnitude (a) and phase (b) of Z_{in} for $l/\lambda = 1.5$, characteristic impedance of the material in magnitude (c) and phase (d), and magnitude (e) and phase (f) of $1/\tanh(\Phi)$ for $l/\lambda = 1.5$. Asterisks indicate the points fulfilling the perfect matching condition of Eq. (5) for $l/\lambda = 1.5$, and the ENZ, ENA, and HE regions are marked.

B. Infinitely thin lossy material slab terminated in a reflector at normal incidence

As we have noted, for $\varepsilon' \to \infty$ one can find perfect absorption peaks that obey the next relations (see the derivations in [36], SI.A):

$$\varepsilon'' \approx \frac{\lambda}{\pi l}, \tag{6}$$

$$\tan(k_0 l n_1) \approx -\frac{n_1}{n_2^2}\frac{\lambda}{2\pi l}, \tag{7}$$

where n_1 and n_2 are, respectively, the real and imaginary parts of the refractive index ($n = \sqrt{\varepsilon}$). While Eq. (6) indicates the asymptotic value that ε'' approaches for large ε', Eq. (7) specifies the sampling of this asymptotic value, corresponding to the locations of absorption peaks. This is determined by the periodicity of the tangent function. Both phenomena are readily visible with the asterisks of Figs. 2 and 3.

As a limiting case, it is found that both equations still hold for slabs of infinitesimal thickness, i.e., when l/λ tends to 0, provided ε' is sufficiently high. In that case, one can always find a value for ε'' from Eq. (6) and determine the value of ε' solving Eq. (7). As demonstrated in Figs. 4(a)–4(c), it is possible to find perfect absorption peaks even for ultrathin slabs at the cost of high real and imaginary parts of ε. This type of regime can be achieved, for instance, near the resonance of dispersive materials characterized by Lorentz dispersion in which both ε' and ε'' can take high values. This will be corroborated in a subsequent section when the analysis is particularized to a slab of SiC.

C. Infinitely thin lossy material slab terminated in a reflector at oblique incidence

In this section, we analyze the angular dependence by extending the TL model to oblique incidence [35]. In this method, first the propagation angle inside the SiC slab is calculated applying Snell's law:

$$\theta = \arcsin\left(\frac{\sin(\theta_0)}{\sqrt{\epsilon}}\right). \tag{8}$$

The complex propagation constant in the normal direction is then calculated as

$$\gamma' = \gamma\cos(\theta). \tag{9}$$

The characteristic impedance of each TL section is determined for the two primary polarizations, namely transverse magnetic (TM) and transverse electric (TE), where the magnetic and electric fields are perpendicular to the incidence plane, respectively:

$$\overline{Z_{\text{TM}}} = \frac{1}{\sqrt{\varepsilon}}\frac{\cos(\theta)}{\cos(\theta_0)}, \tag{10}$$

$$\overline{Z_{\text{TE}}} = \frac{1}{\sqrt{\varepsilon}}\frac{\cos(\theta_0)}{\cos(\theta)}. \tag{11}$$

These values are introduced in the TL model, and the absorbance is then calculated using the same methodology as before, namely

$$\overline{Z_{\text{TM,TE}}} = \coth(\gamma' l). \tag{12}$$

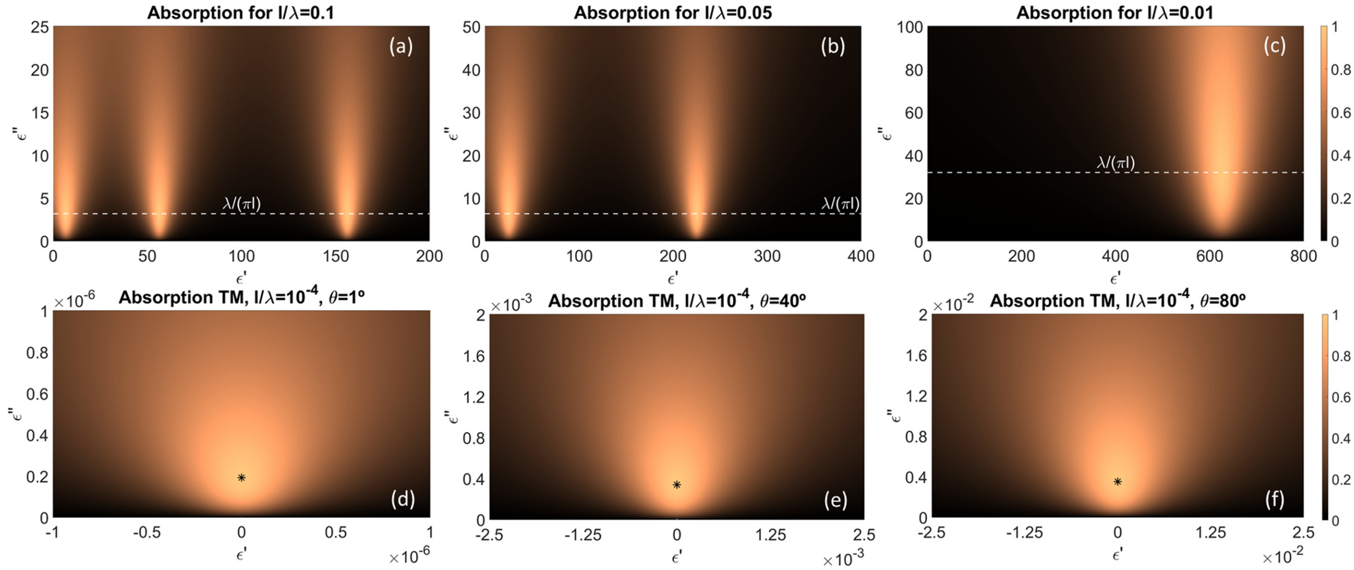

FIG. 4. Absorption color maps for different permittivity combinations for $l/\lambda = 0.1$ (a), 0.05 (b), and 0.01 (c), and absorption maps for a thin slab of $l/\lambda = 10^{-4}$ for TM mode when the angle of incidence is 1° (d), 40° (e), and 80° (f). In (d)–(f), the solutions are located in the ENZ region where TE mode is omitted due to lack of absorption, and black asterisks mark the predictions of Eqs. (13) and (14).

In general, this equation admits infinite solutions for different combinations of thickness, permittivity, and incidence angle. A case of special interest arises again when we take the limit of infinitesimal thickness ($l/\lambda \to 0$) while considering moderate values (i.e., not tending to infinite) of $\varepsilon', \varepsilon''$ (see [36], SI.B). Interestingly, perfect absorption cannot happen under TE incidence (see the demonstration in [36], SI.B), whereas for TM polarization we find that peaks can be found for the next permittivity values:

$$\varepsilon' \approx [k_0 l \tan(\theta_0)]^2, \tag{13}$$

$$\varepsilon'' \approx k_0 l \sin(\theta_0) \tan(\theta_0). \tag{14}$$

From the previous equations, we find that for small angles of incidence, the solutions for both ε' and ε'' tend to zero, indicating that an absorption peak for ultrathin slabs near normal incidence happens at the strict ENZ condition; see Fig. 4(d). For larger angles of incidence [Fig. 4(e)] even approaching grazing incidence [Fig. 4(f)], solutions exist for higher permittivity values. Although the values of ε' and ε'' are larger than at normal incidence, one condition is $\varepsilon' \ll \sin(\theta_0)$ (see [36], SI.B), so these solutions always happen within the ENZ regime. It is noteworthy that even with an ultrathin slab ($l/\lambda = 10^{-4}$) and $\theta_0 = 80^\circ$, a perfect absorption peak is obtained for a value of $\varepsilon'' \approx 0.4\times10^{-2}$. Furthermore, it is found that ε' is generally smaller than ε'' due to the $(k_0 l)^2$ term. Finally notice that at $\theta_0 = 0^\circ$ only a trivial solution is found with both ε' and ε'' equal to zero, which obviously cannot produce any absorption peak. This is the reason why our previous analysis did not find any solution in the ENZ region at normal incidence for ultrathin slabs. Note also that this is not in contradiction with the results of the previous section since we consider here only moderate values of permittivity, whereas in the previous study we considered high values of ε'. Similarly, at strictly $\theta_0 = 90^\circ$ the solutions diverge.

D. Generic lossy material slab separated by a dielectric spacer from a reflector

An interesting extension of the previous structure is achieved by inserting an air layer, or any other lossless dielectric, of length l_s between the material and the PEC, as depicted in Fig. 5(a). Such a dielectric spacer will be considered also nonmagnetic ($\mu = 1$) and with a constant, positive real-valued relative permittivity ε_s. According to Eqs. (1) and (2), this medium can be modeled as a lossless TL section with $Z_s \in \mathbb{R}$ and $\gamma_s = j\beta_s$. Therefore, the overall equivalent circuit consists of two concatenated transmission lines terminated in a short circuit, as illustrated in Fig. 5(b). Assuming again $Z_L = 0\ \Omega$, the input impedance of the total system can be calculated from Eq. (15):

$$\overline{Z_{\rm in}} = \overline{Z}\frac{\overline{Z_1} + \overline{Z}\tanh(\Phi)}{\overline{Z} + \overline{Z_1}\tanh(\Phi)}, \tag{15}$$

where $\overline{Z_1} = j\overline{Z_s}\tan(\Phi_s)$ and $\Phi_s = \beta_s l_s$. The addition of a spacer introduces a modification of the terminal impedance seen by the top material. Now $\overline{Z_1}$ depends both on the spacer thickness l_s and permittivity ε_s, as represented in Fig. 5(c). An important consideration is that when ε_s has a real value, $\overline{Z_1}$ is purely imaginary. As depicted in Fig. 5(c) for two different values of ε_s (1 and 4), when $l_s/\lambda < 1/4$, $\overline{Z_1}$ is inductive, with its magnitude increasing as l_s/λ increases. At $l_s/\lambda = 1/4$, $\overline{Z_1}$ becomes an open circuit, diverging to infinity. For $1/4 < l_s/\lambda < 1/2$, $\overline{Z_1}$ becomes capacitive, and at $l_s/\lambda = 1/2$ it behaves as a short circuit. This pattern repeats periodically for larger values of l_s/λ, with a period of 1/2.

Similar to the previous scenario, we conducted an analytical investigation by mapping the absorbance of the material on the top of the structure as a function of ε' and ε'', where ε' varies from -5 to 15 and ε'' ranges from 0 to 5. This analysis was performed for different values of l/λ and l_s/λ, spanning from 0.1 to 2. Without loss of generality, an air layer ($\varepsilon_s = 1$)

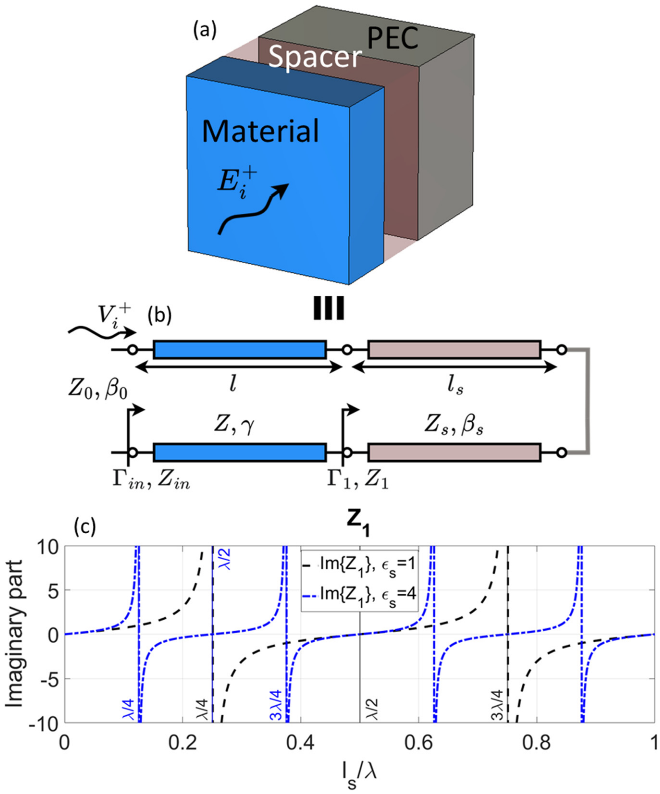

FIG. 5. (a) Structure of a generic material separated from a PEC with a dielectric spacer, (b) equivalent circuit of the structure, and (c) load impedance seen by the material as a function of length and permittivity of the spacer, where vertical lines mark the values of $l_s = \frac{\lambda}{4}, \frac{\lambda}{2}, \frac{3\lambda}{4}$.

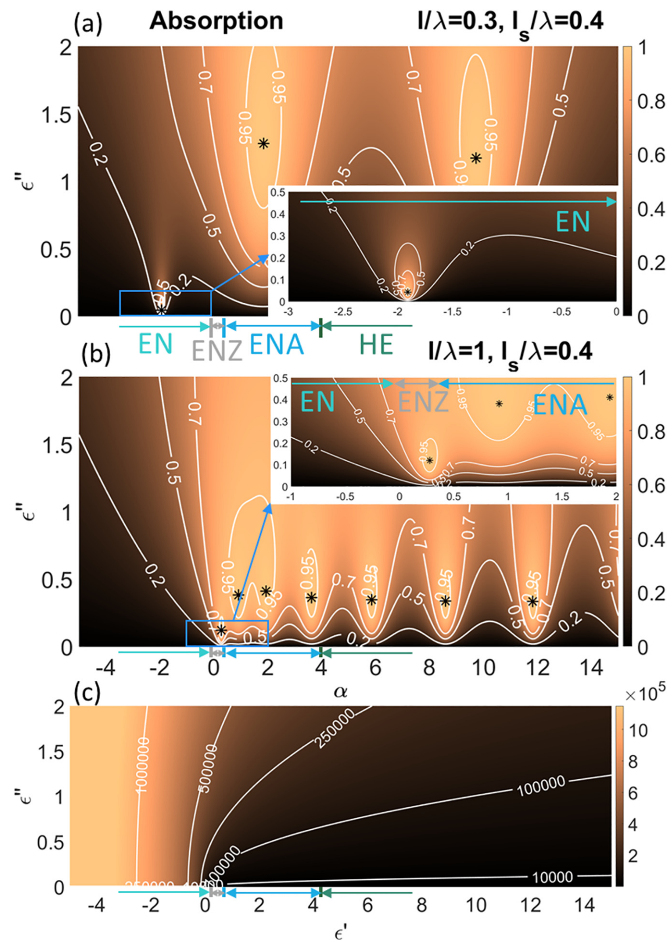

FIG. 6. Absorption color maps for (a) $l/\lambda = 0.3$ and $l_s/\lambda = 0.4$, and for (b) $l/\lambda = 1$ and $l_s/\lambda = 0.4$. Panel (c) presents the attenuation constant of the material over ε, where $\varepsilon' < 0$ imply higher propagation losses. Regions of epsilon-negative (EN, $\varepsilon' < 0$), ENZ, ENA, and HE are indicated, and black asterisks mark perfect matching condition points.

is considered for the spacer, so that $\overline{Z_1}$ coincides with the black curve of Fig. 5(c). Some selected results for different combinations of thicknesses are presented in Fig. 6 to grasp the behavior of the whole device.

Figure 6 shows absorption bands when $\varepsilon' > 0$ similar to the ones presented in Figs. 3(a)–3(c). An intuitive explanation for this effect is that the unbounded oscillatory behavior of $\tanh(\Phi)$ allows for a wide range of potential impedance matching conditions within this regime, as long as a minimum l is maintained. Consequently, despite the new load impedance introduced by the spacer, as observed in Fig. 5(c), the overall trend of impedance matching persists, albeit with shifted locations.

Interestingly, the inset picture of Fig. 6(a) displays an absorption peak located at negative values of ε' ($\varepsilon' \approx -1.9$) opening a new domain of solutions. Furthermore, this isolated resonance in the negative permittivity region contrasts with the periodic resonances observed when $\varepsilon' > 0$, suggesting a fundamentally distinct physics. To gain further insight into this effect, it is crucial to examine the behavior of $\overline{Z}$, $\coth(\Phi)$, and $\overline{Z_1}$. As mentioned in the previous section, when $\varepsilon' < 0$ the imaginary part of the impedance dominates over its real part, and $\coth(\Phi)$ approaches 1 asymptotically. Therefore, from Eq. (15) and knowing that the positive imaginary part of $\overline{Z}$ must be compensated to get $\overline{Z_{\text{in}}} = 1$, the only viable solution in this case is for $\overline{Z_1}$ to be a complex number with a negative imaginary part, i.e., with a capacitive reactance. This happens for $(2n+1)\frac{\lambda}{4} < \Phi_s < (n+1)\frac{\lambda}{2}, \ \forall n \in \mathbb{N}$. Additionally, as $\coth(\Phi)$ exhibits no oscillations in this range, only a single solution exists.

The absence of this absorption peak in Fig. 6(b) indicates that more conditions must be fulfilled. In fact, as the top material has negative permittivity, losses are higher [see Fig. 6(c)], and therefore the thickness of the material is critical. If the slab is too thick, the energy decays inside the block and never reaches the air layer so that it looks to the incident wave like a semi-infinite slab. Thus, the matching condition is lost, and part of the energy is reflected at the input interface without giving rise to an absorption peak. Conversely, if the slab is too thin, insufficient losses will hinder perfect absorption, and the matching condition cannot be reached.

Two extreme cases are identified when $\overline{Z_1}$ is capacitive. First, when l_s approaches $n\lambda/2$ from lower values, $\overline{Z_1}$ tends to become slightly negative (0^-). To compensate for this small negative imaginary load impedance, a material with a small positive imaginary part impedance is needed. This implies the necessity of a negative ε' with a large magnitude. Secondly,

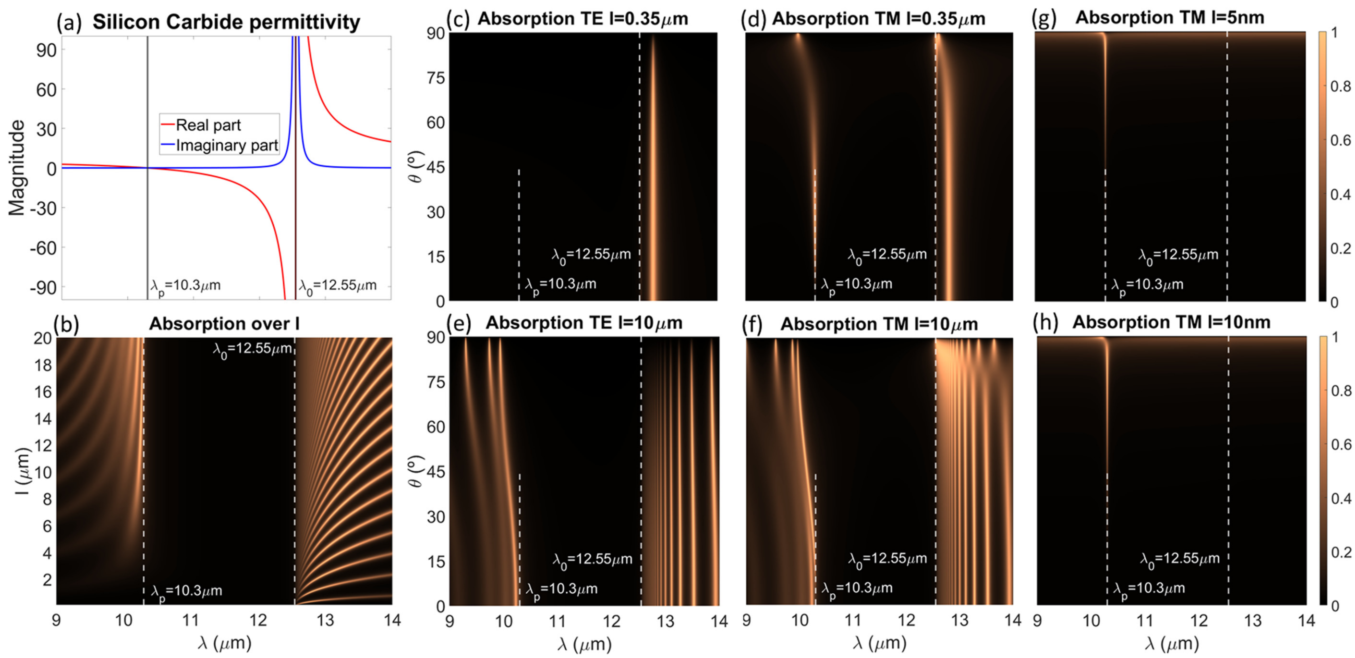

FIG. 7. (a) Permittivity curve of silicon carbide (SiC). (b) Absorption map over λ and l for normal incidence. Absorption maps over λ and θ for $l = 0.35$ μm (c),(d) and $l = 10$ μm (e),(f) with TE and TM incidence. Panels (g),(h) depict these maps for $l = 5$ and 10 nm under TM incidence. Both plasma and resonance wavelengths are marked.

when l_s approaches $(2n+1)\lambda/4$, $\overline{Z_1}$ tends toward negative infinity. In this case, a material with a large positive imaginary part impedance is required. Consequently, ε' should approach zero while still being negative. Nevertheless, both regimes will require different material thicknesses as they imply very different absorption rates. For permittivity values near zero and negative (referred to as negative ENZ), a thicker thickness is required due to reduced losses [see Fig. 6(c)]. This stands in sharp contrast to the negative counterpart of the HE regime, where higher ε' values indicate higher losses and therefore require a thinner l. Hence, the connection between ε and l is reciprocal and inversely related. As the magnitude of ε' increases, both l and $\overline{Z_1}$ must decrease in order to get impedance matching, while the opposite holds true for lower ε'. Then, once the material's permittivity is known, one can design the dimensions accordingly to get perfect absorption peaks using a wide range of materials.

III. DISPERSIVE MATERIAL IMPLEMENTATION

Up to this point, we have established the general conditions for generating absorption peaks as a function of the complex permittivity of a generic material slab. Now, in pursuit of a more practical approach, we analyze the performance using a slab of silicon carbide (SiC) and with aluminum instead of PEC for the bottom reflector, with a permittivity extracted from [37,38]. SiC is chosen for the slab because it has a dispersive permittivity that covers all the regions previously discussed in a relatively small bandwidth in the infrared region. Its relative permittivity is characterized by a Drude-Lorentz model [39],

$$\varepsilon_{\mathrm{SiC}} = \varepsilon_\infty \frac{\omega^2 - \omega_p^2 - j\omega\omega_c}{\omega^2 - \omega_0^2 - j\omega\omega_c} \tag{16}$$

with the following parameters: resonance frequency $\omega_0 = 1.50\times10^{14}$ rad/s, plasma frequency $\omega_p = 1.83\times10^{14}$ rad/s, collision frequency of $\omega_c = 0.0022\omega_0$, and a permittivity at infinity of $\varepsilon_\infty = 5.726$. As represented in Fig. 7(a), at $\lambda = 10.3$ μm we have $\varepsilon'_{\mathrm{SiC}} = 0$, with a dielectric region below that wavelength and a plasma region above. At $\lambda = 12.55$ μm, $\varepsilon'_{\mathrm{SiC}}$ tends to infinity, with a plasma region below such a point and a dielectric above.

A. Silicon carbide slab ended in an aluminum reflector

The setup considered here is the same as the one in Fig. 1 but replacing the blue generic material by SiC and the PEC by aluminum (a similar analysis using PEC is presented in [36], SII with similar results).

In the initial study we analyze the resonance modes that lead to absorption peaks as well as their bandwidth, varying the thickness of the SiC slab from 0.1 to 20 μm and λ between 9 and 14 μm. The absorbance results are plotted in Fig. 7(b) as a color map, where λ_p and λ_0 of SiC are explicitly highlighted. In good agreement with our previous analysis, the absorption peaks appear only for positive values of $\varepsilon'_{\mathrm{SiC}}$. In addition to this, strong resonances appear both in the ENZ region and on the right side of the Lorentz resonance (HE region).

Figure 7(b) shows the results at normal incidence. As depicted there, the peaks below 10.3 μm start to have an absorption above 90% for $l > 11$ μm and completely disappear for $l < 4$ μm. These findings are consistent with the previous discussion about the minimum thickness to get high absorption at normal incidence in the ENZ regime. As an example, with $l = 12$ μm, the device absorbs 95% of the incident power with a full width at half-maximum bandwidth of 0.566%. Furthermore, as l increases, several new absorption modes appear, as predicted in Fig. 2. The electric field distribution inside the SiC slab corresponds to an electric length of approximately $l = n\lambda/2$ (see [36], SIII).

On the left side of the ENZ band lies the ENA ($0.4 < \varepsilon'_{\mathrm{SiC}} < 4$) region, which begins below $\lambda = 10.175$ μm for SiC. In this region, faint absorption peaks appear, becoming stronger for thick slabs but not as intense as in the ENZ region. This can be explained by observing that $\varepsilon''_{\mathrm{SiC}} < 0.027$ within this band, which is a value relatively low to get significant absorption (see Fig. 2). Nevertheless, the absorption level increases as l increases because the perfect matching condition requires lower values of $\varepsilon''_{\mathrm{SiC}}$ for higher thicknesses [compare Figs. 2(a)–2(c)].

Regarding the behavior near the Lorentz resonance (HE regime), the absorption in this region starts for very small thicknesses, as we already found in our previous discussion on ultrathin slabs at normal incidence. Absorbance values exceeding 99.9% can be achieved with a thickness as low as 260 nm resulting in an extremely narrow full width at half-maximum bandwidth of 0.43%. As discussed in the previous section, by having a higher ε' and ε'', the thickness could be further reduced [check Eqs. (6) and (7)].

Next, we analyze the angular dependence by extending the TL model to oblique incidence following the method explained in Sec. II C [34]. Using Eqs. (8)–(12), we computed the response varying the incidence angle θ between 0° and 89° for the two principal polarizations (the field distributions are shown in [36], SIII). The absorption maps over λ and θ are shown in Figs. 7(c)–7(f) for $l = 0.35$ and 10 μm. These two cases have been chosen to highlight the differences between thin and thick slabs.

As depicted in Figs. 7(c) and 7(d) for small values of thickness ($l = 350$ nm), the response near the ENZ resonance depends strongly on the polarization and angle. As discussed above, absorption peaks at oblique incidence cannot exist under TE incidence, whereas a clear absorption band arises under TM polarization for θ between 8° and 60°. Note that for $\theta < 8°$ the absorption peak vanishes. This happens because for small incidence angles the values of both ε' and ε'' must be extremely small, as demonstrated by Eqs. (13) and (14), and SiC has no combinations that approach those values. For $l = 10$ μm [Figs. 7(e) and 7(f)], the perfect absorption peak near the ENZ regime for small angles shifts towards lower λ values as θ increases, entering the ENA region. This is explained by the impedance matching condition over θ (see [36], SI.C). Remarkably, perfect absorption occurs for very high incidence angles for both polarizations at different locations due the different matching condition for TE and TM polarization (see [36], SI.C).

Now we study perfect absorption for ultrathin slabs, following the general explanation presented in Sec. II C. Figures 7(g) and 7(h) illustrate the absorption for TM polarization as a function of incidence angle (θ) for extremely small thicknesses, $l = 5$ and 10 nm. As l is reduced, the perfect matching condition shifts toward higher incidence angles within the ENZ region following Eqs. (13) and (14). Eventually, a near-perfect absorption of 99.54% is achieved for $l = 5$ nm, $\theta = 84°$ and $\lambda = 10.35$ μm, where even the solution for the Lorentz resonance has vanished. Absorption in anisotropic ENZ media at grazing angles has already been theoretically analyzed without polarization discrimination in [33], but our results show that both anisotropy and grazing angle incidence are not necessary to get absorption in ultrathin slabs. In fact, by operating near the ENZ regime under TM incidence, one can find absorption peaks at any angle of incidence except for 0° and 90°. However, in practice, absorption peaks are more prone to be found at large angles of incidence, as they need larger values of ε'', which are easier to find in practical materials.

Regarding the HE regime near the Lorentz resonance region ($\lambda = 12.55$ μm), the absorption peak locations are robust with respect to the angle variation for both thicknesses [see Figs. 7(c)–7(f)]. Comparing Figs. 7(e) and 7(f), TE and TM modes only differ for angles above 60° due to their different matching condition, where TM has a strong absorption with high angles of incidence in a broader bandwidth (see [36], SI.C).

B. Adding a dielectric spacer between the silicon carbide and the aluminum reflector

Now we examine the scenario depicted in Fig. 5(a), considering the material of the blue slab as SiC and the PEC as an aluminum plane. Initially, we conduct a sweep of l and l_0, varying from 0.1 to 20 μm, to ascertain the location of the absorption bands across the wavelength range of $9 - 14$ μm. Subsequently, we study the angular dependence for both TE and TM polarizations. The results are depicted in Fig. 8.

An absorption map over l and with fixed $l_0 = 4$ μm is presented in Fig. 8(a). When $\varepsilon'_{\mathrm{SiC}} > 0$, i.e., below λ_p and above λ_0, a pattern similar to that presented in Fig. 7(b) is observed, with some shifts in the resonances due to the additional phase introduced by the spacer. Even the bandwidth and the absorption rates are practically identical.

The value chosen for l_0 is between $\lambda/4$ and $\lambda/2$, which, following our previous discussion, admits solutions in the plasma region of SiC. Hence, a strong absorption peak is observed when $\varepsilon'_{\mathrm{SiC}} < 0$ around $\lambda = 10.6$ μm. This case is similar to a metal-dielectric-metal Salisbury screen. As expected, this resonance depends strongly on l and does not have harmonic solutions, whereas the wavelength location remains constant for the few values of l that fulfill the matching condition.

The absorption map over l_0 with fixed $l = 2$ μm is depicted in Fig. 8(b). The periodicity for the resonances in the negative and high permittivity regions correspond approximately to $l_0 = n\lambda/2$. Both cases are easily explained by the periodicity of the load impedance seen by the SiC slab [see Fig. 5(c)].

The angle and polarization dependencies are depicted in Figs. 8(c)–8(e) for $l = 1.5$ and 5 μm. These dimensions have been selected to better explain all the phenomena occurring in the device. The information about the field distribution is discussed in [36], SIV. For small values of l, there is only absorption for the TM mode in the ENZ region, again with robustness with the angle between 5° and 35°; see Fig. 8(d). The region around the Lorentz resonance has a similar tendency to that shown in Figs. 7(c)–7(f) and discussed in the previous section.

We focus then on the new resonance that appears in the plasma region of SiC, between λ_p and λ_0. At $\theta = 0°$, this configuration achieves an absorption of 94% within an extremely narrow bandwidth of less than 0.4%. In contrast to the

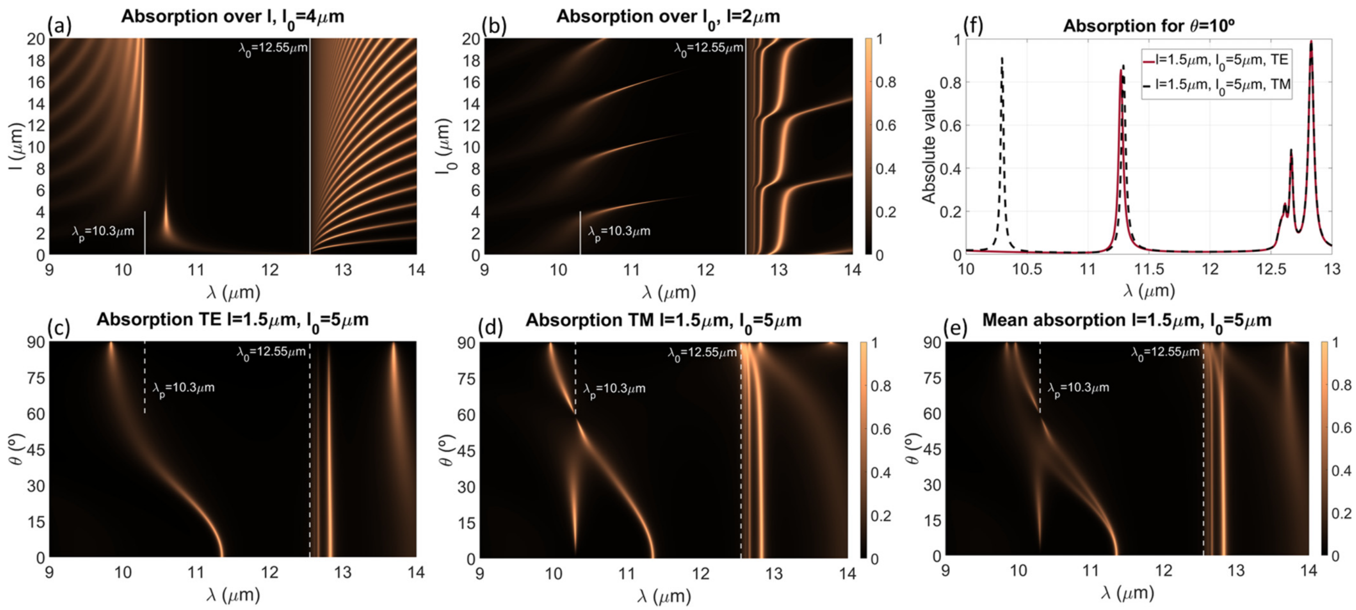

FIG. 8. Absorption maps over (a) SiC length l and (b) over the air spacer length l_0 for each wavelength. The absorption for orthogonal polarization modes (c) TE and (d) TM over θ and λ. Panel (e) shows the total absorption with a strong polarization discrimination for high angles, and (f) is an example of a triple ultra-narrow-band absorber selecting $l = 1.5$ μm and $l_0 = 5$ μm.

absorption peaks previously examined, this resonance demonstrates a clear angular dependency, with an observed decrease in the absorption wavelength as θ increases. In contrast to conventional Salisbury screens, SiC introduces polarization discrimination over a range of angles due to the different characteristic impedance of TE and TM modes. For both polarizations, as the angle increases, the absorption peak shifts towards shorter wavelengths until it reaches the point where $\varepsilon'_{\mathrm{SiC}} = 0$, after which it continues to exhibit absorption for positive permittivity values. Additionally, Fig. 8(e) shows that the absorption peaks take place at different wavelengths for TE and TM polarization from $\theta = 15^\circ$ and above.

An interesting point appears under TM polarization in Fig. 8(d) for $\lambda = 10.3$ μm and $\theta = 59^\circ$, where the Salisbury screen mode hybridizes with the ENZ mode (see [36], SIV). This hybridization causes a total reflection at this point, canceling the trend of perfect absorption associated with the Salisbury-screen-like mode. Additionally, there is notable absorption at high incidence angles in the HE region for the TE mode, which were absent in Fig. 7(c).

It is important to note that the dispersion of the material can be exploited in these setups to attain multiband operation. In Fig. 8(f), we represent the specific case at $\theta = 10^\circ$ for $l = 1.5$ μm and $l_0 = 5$ μm, revealing a triple ultra-narrow-band absorber based on the ENZ, NE, and HE regimes, each associated with different absorption phenomena. This further highlights the potential of using material dispersion instead of adding complex geometries to the structure for multiband operation.

IV. CONCLUSIONS

In this paper, we explored various approaches to attain ultranarrow absorption peaks based on the complex permittivity of a single slab. We focused on two simple scenarios: a slab placed on a reflector, and a slab separated from the reflector by a dielectric layer. We chose these scenarios for their simplicity, as they are photolithography-free and avoid complex multilayer structures.

We began using TL theory to demonstrate all possible solutions for perfect absorption of an arbitrary material on top of a reflector. Although simple, this analysis provides insights for designing perfect absorbers exploiting the permittivity regions described in the paper: ENZ ($\varepsilon' < 0.4$), ENA ($0.4 < \varepsilon' < 4$), and HE ($\varepsilon' > 4$). Some general conclusions can be drawn from the analysis. First, the relationship between thickness and permittivity, as governed by the perfect matching condition, enables a wide range of materials and dimensions that can be adjusted to achieve absorption peaks at an arbitrary wavelength. Second, a dispersive material [$\varepsilon = \varepsilon(\lambda)$] operating near the ENZ regime can have an ultra-narrow-band absorption with some minimum thickness requisite. This happens due to the rapid disappearance of the matching condition with minimal variation in permittivity within the ENZ region. On the contrary, a material with a permittivity within the ENA region could be better suited for broadband absorbers, since the matching condition is more robust to permittivity variations. Finally, in this regard, HE materials possess mixed properties between these two regions, but without thickness requirements as long as permittivity is high enough.

In a subsequent study, we found that under the approximation of high ε', there exists an asymptotic solution for ε'' proportional to λ/l. This finding has a notable implication as it presents the feasibility of having ultrathin absorbers provided that the permittivity attains a sufficiently high value. This phenomenon can be found in dispersive materials characterized by Lorentz dispersion, where both ε' and ε'' reach high levels.

The analysis was then extended to oblique incidence. Multiple solutions are possible in any of the ENZ, ENA, or HE regions, expanding the reach of normal incidence. An intriguing observation arises when the analysis is particularized to ultrathin slabs: under TM incidence, solutions appear in the ENZ region for any angle of incidence except 0° and 90°, while no solution exists under TE incidence. Explicit expressions for both ε' and ε'' were derived proving that near the ENZ region, a stable absorption peak for any angle can be obtained.

Then, we extrapolated the analysis to an arbitrary material separated with a dielectric spacer from the reflector. It was found that the incorporation of a dielectric layer introduces a new level of flexibility to the design of perfect absorbers. A new absorption regime within the negative ε' region appears while all the absorption phenomena of a material with positive ε' on top of a reflector are maintained. The new resonance mode can be tuned in terms of both its location and width, allowing for the generation of absorption peaks as narrow as those found in the ENZ region with the previous setup. This can be accomplished without the necessity of imposing a minimum value on the slab thickness, but with a spacer length between $\lambda/4$ and $\lambda/2$. This suggests that for dispersive materials exhibiting a transition from negative to positive values of the real permittivity, various physical mechanisms can be utilized to achieve absorption peaks. Moreover, the material dispersion can be leveraged to design multiband absorbers exploiting the different regimes.

Seeking a more practical implementation, the different setups were studied by using a SiC slab as dispersive material. We obtained the bandwidth, and we studied the angle dependence and polarization response, leading in the best case to ultra-narrow-band absorption above 99% with a relative bandwidth of less than 0.4%. We could corroborate our main findings of the general analysis with absorption peaks present in all the operation regions for sufficiently thick slabs. It is relevant that we could observe peaks in both extreme ENZ and HE regions at normal incidence. We could confirm the presence of peaks in the HE region for ultrathin slabs in agreement with our previous theoretical derivations. In the case of ENZ absorption, a thicker slab is necessary at normal incidence, also predicted in our analysis. The peak is robust with λ and can achieve a relative bandwidth of 0.566%. In concordance with our previous analysis, ENZ absorption exists at oblique incidence only for TM polarization and its magnitude has some dependence with the angle. We also showed that an ultrathin nanometric slab has perfect absorption at high incidence angles in the ENZ regime. HE absorption is more robust with angle and needs thinner slabs, but it is strongly dependent on λ and it leads to multiple cavity modes for thick slabs.

Lastly, we studied the behavior of a SiC slab separated with a dielectric spacer from the reflector. All the absorption phenomena of the device without the spacer are maintained, while allowing absorption in the NE region of the silicon carbide, mimicking a Salisbury screen. Even more, this last absorption mode can be hybridized with the TM mode in the ENZ region, resulting in perfect reflection at specific incidence angles. The TE mode exhibits strong emission at high angles in high epsilon regimes. We also demonstrated how to exploit SiC dispersion to achieve a triple ultra-narrow-band absorber. Nevertheless, the increased complexity introduced by the spacer makes developing exact and easy design relations challenging. Using current research on optimization techniques applied to light manipulation could improve such a design [40–42]. This approach to dispersion is applicable to any polar dielectric, and it could be extended to 3D scatterers [43] using a different formalism for the theoretical analysis.

We acknowledge that this study is limited to smooth surfaces. In practical applications, surface roughness can lead to a modification of the impedance matching as well as an increased absorption with reduced selectivity in wavelength, with ultrathin slabs being particularly susceptible. Nevertheless, surface roughness in ENZ media of a few nanometers keeps the response reasonably unchanged [44]. This work presents a valuable in-depth analysis of the simplest multilayer absorbers, and it identifies some special regimes that lead to absorption in ultrathin slabs, bringing insights and predicting a few phenomena that have been overlooked in the literature and that can be extrapolated to common reflective metals as substrate.

ACKNOWLEDGMENTS

The research presented in this paper has been supported by funding from the European Union's Horizon 2020 research and innovation program under Grant Agreement No. 964450 (MIRACLE project, more information available in Ref. [45]) from the EU Commission. Additionally, this work has received financial support from Project No. TED2021-132074B-C33, funded by MCIN/AEI/10.13039/501100011033, and the European Union NextGenerationEU/PRTR and from Project No. PID2022-137845NB-C21, funded by MCIN/AEI/10.13039/501100011033 and by FEDER Una manera de hacer Europa. C.L. acknowledges financial support from Santander Bank and Public University of Navarra under resolution 2659/2021.

[1] H. Daneshvar, R. Prinja, and N. P. Kherani, Thermophotovoltaics: Fundamentals, challenges and prospects, Appl. Energy **159**, 560 (2015).

[2] Z. Zhou, E. Sakr, Y. Sun, and P. Bermel, Solar thermophotovoltaics: reshaping the solar spectrum, Nanophotonics **5**, 1 (2016).

[3] X. Yu, J. Chan, and C. Chen, Review of radiative cooling materials: Performance evaluation and design approaches, Nano. Energy **88**, 106259 (2021).

[4] Z. Ding, L. Pattelli, H. Xu, W. Sun, X. Li, L. Pan, J. Zhao, C. Wang, X. Zhang, Y. Song, J. Qiu, Y. Li, and R. Yang, Iridescent daytime radiative cooling with no absorption peaks in the visible range, Small **18**, 2202400 (2022).

[5] J. Yang, X. Zhang, X. Zhang, L. Wang, W. Feng, and Q. Li, Beyond the visible: Bioinspired infrared adaptive materials, Adv. Mater. **33**, 2004754 (2021).

[6] N. N. Shi, C.-C. Tsai, F. Camino, G. D. Bernard, N. Yu, and R. Wehner, Keeping cool: Enhanced optical reflection and

radiative heat dissipation in saharan silver ants, Science **349**, 298 (2015).
[7] D. Rodrigo, O. Limaj, D. Janner, D. Etezadi, F. J. G. de Abajo, V. Pruneri, and H. Altug, Mid-infrared plasmonic biosensing with graphene, Science **349**, 165 (2015).
[8] N. Liu, M. Mesch, T. Weiss, M. Hentschel, and H. Giessen, Infrared perfect absorber and its application as plasmonic sensor, Nano Lett. **10**, 2342 (2010).
[9] D. Benedikovic, L. Virot, G. Aubin, J.-M. Hartmann, F. Amar, X. L. Roux, C. Alonso-Ramos, É. Cassan, D. Marris-Morini, J.-M. Fédéli, F. Boeuf, B. Szelag, and L. Vivien, Silicon-germanium receivers for short-wave-infrared optoelectronics and communications, Nanophotonics **10**, 1059 (2021).
[10] Z. M. Abd El-Fattah, V. Mkhitaryan, J. Brede, L. Fernández, C. Li, Q. Guo, A. Ghosh, A. R. Echarri, D. Naveh, F. Xia, J. E. Ortega, and F. J. García de Abajo, Plasmonics in atomically thin crystalline silver films, ACS Nano **13**, 7771 (2019).
[11] E. J. C. Dias, R. Yu, and F. J. García de Abajo, Thermal manipulation of plasmons in atomically thin films, Light: Sci. Appl. **9**, 87 (2020).
[12] J. Hu, Y. Hu, Y. Ye, and R. Shen, Unique applications of carbon materials in infrared stealth: A review, Chem. Eng. J. **452**, 139147 (2023).
[13] A. Shahsafi, P. Roney, Y. Zhou, Z. Zhang, Y. Xiao, C. Wan, R. Wambold, J. Salman, Z. Yu, J. Li, J. T. Sadowski, R. Comin, S. Ramanathan, and M. A. Kats, Temperature-independent thermal radiation, Proc. Natl. Acad. Sci. USA **116**, 26402 (2019).
[14] S. Yang, J. Wang, G. Dai, F. Yang, and J. Huang, Controlling macroscopic heat transfer with thermal metamaterials: Theory, experiment and application, Phys. Rep. **908**, 1 (2021).
[15] H. Wei, J. Gu, F. Ren, L. Zhang, G. Xu, B. Wang, S. Song, J. Zhao, S. Dou, and Y. Li, Smart materials for dynamic thermal radiation regulation, Small **17**, 2100446 (2021).
[16] M. A. Kats, R. Blanchard, S. Zhang, P. Genevet, C. Ko, S. Ramanathan, and F. Capasso, Vanadium dioxide as a natural disordered metamaterial: Perfect thermal emission and large broadband negative differential thermal emittance, Phys. Rev. X **3**, 041004 (2013).
[17] Z. Li, S. Butun, and K. Aydin, Large-area, lithography-free super absorbers and color filters at visible frequencies using ultrathin metallic films, ACS Photon. **2**, 183 (2015).
[18] M. A. Naveed, R. M. H. Bilal, M. A. Baqir, M. M. Bashir, M. M. Ali, and A. A. Rahim, Ultrawideband fractal metamaterial absorber made of nickel operating in the uv to ir spectrum, Opt. Express **29**, 42911 (2021).
[19] G. M. Akselrod, J. Huang, T. B. Hoang, P. T. Bowen, L. Su, D. R. Smith, and M. H. Mikkelsen, Large-area metasurface perfect absorbers from visible to near-infrared, Adv. Mater. **27**, 8028 (2015).
[20] C. Yang, C. Ji, W. Shen, K.-T. Lee, Y. Zhang, X. Liu, and L. J. Guo, Compact multilayer film structures for ultrabroadband, omnidirectional, and efficient absorption, ACS Photon. **3**, 590 (2016).
[21] T. Ozawa, H. M. Price, A. Amo, N. Goldman, M. Hafezi, L. Lu, M. C. Rechtsman, D. Schuster, J. Simon, O. Zilberberg, and I. Carusotto, Topological photonics, Rev. Mod. Phys. **91**, 015006 (2019).
[22] P. Lova, G. Manfredi, and D. Comoretto, Advances in functional solution processed planar 1d photonic crystals, Adv. Opt. Mater. **6**, 1800730 (2018).
[23] X. Niu, X. Hu, S. Chu, and Q. Gong, Epsilon-near-zero photonics: A new platform for integrated devices, Adv. Opt. Mater. **6**, 1701292 (2018).
[24] S. Campione, D. de Ceglia, M. A. Vincenti, M. Scalora, and F. Capolino, Electric field enhancement in ε-near-zero slabs under tm-polarized oblique incidence, Phys. Rev. B **87**, 035120 (2013).
[25] M. Koivurova, T. Hakala, J. Turunen, A. T. Friberg, M. Ornigotti, and H. Caglayan, Metamaterials designed for enhanced enz properties, New J. Phys. **22**, 093054 (2020).
[26] J. Rensberg, Y. Zhou, S. Richter, C. Wan, S. Zhang, P. Schöppe, R. Schmidt-Grund, S. Ramanathan, F. Capasso, M. A. Kats, and C. Ronning, Epsilon-near-zero substrate engineering for ultrathin-film perfect absorbers, Phys. Rev. Appl. **8**, 014009 (2017).
[27] L. Cai, K. Du, Y. Qu, H. Luo, M. Pan, M. Qiu, and Q. Li, Nonvolatile tunable silicon-carbide-based midinfrared thermal emitter enabled by phase-changing materials, Opt. Lett. **43**, 1295 (2018).
[28] J. M. Pérez-Escudero, I. Buldain, M. Beruete, J. Goicoechea, and I. Liberal, Silicon carbide as a material-based high-impedance surface for enhanced absorption within ultra-thin metallic films, Opt. Express **28**, 31624 (2020).
[29] D. Navajas, J. M. Pérez-Escudero, and I. Liberal, Spectrally stable thermal emitters enabled by material-based high-impedance surfaces, Nanoscale Adv. **5**, 650 (2023).
[30] S. Lee, D. Seo, S. H. Park, N. Izquierdo, E. H. Lee, R. Younas, G. Zhou, M. Palei, A. J. Hoffman, M. S. Jang, C. L. Hinkle, S. J. Koester, and T. Low, Achieving near-perfect light absorption in atomically thin transition metal dichalcogenides through band nesting, Nat. Commun. **14**, 3889 (2023).
[31] J. Horng, E. W. Martin, Y.-H. Chou, E. Courtade, T.-C. Chang, C.-Y. Hsu, M.-H. Wentzel, H. G. Ruth, T.-C. Lu, S. T. Cundiff, F. Wang, and H. Deng, Perfect absorption by an atomically thin crystal, Phys. Rev. Appl. **14**, 024009 (2020).
[32] Y. Long, R. Su, Q. Wang, L. Shen, B. Li, and W. Zheng, Deducing critical coupling condition to achieve perfect absorption for thin-film absorbers and identifying key characteristics of absorbing materials needed for perfect absorption, Appl. Phys. Lett. **104**, 091109 (2014).
[33] S. Feng and K. Halterman, Coherent perfect absorption in epsilon-near-zero metamaterials, Phys. Rev. B **86**, 165103 (2012).
[34] S. Ramo, J. R. Whinnery, and T. V. Duzer, *Fields and Waves in Communication Electronics* (Wiley, Sahibabad, 2013).
[35] S. Vassant, J.-P. Hugonin, F. Marquier, and J.-J. Greffet, Berreman mode and epsilon near zero mode, Opt. Express **20**, 23971 (2012).
[36] See Supplemental Material at http://link.aps.org/supplemental/10.1103/PhysRevB.110.045408 for derivations of equations of Secs. II B and II C; complementary results of perfect absorption over the angle for a material atop a PEC and a silicon carbide slab on top of a PEC; the electromagnetic field distribution for the different absorption peaks of both structures of Sec. III using a PEC as a reflector.
[37] M. N. Polyanskiy, Refractiveindex.info database of optical constants, Sci. Data **11**, 94 (2024).
[38] A. D. Rakić, Algorithm for the determination of intrinsic optical constants of metal films: Application to aluminum, Appl. Opt. **34**, 4755 (1995).

[39] J. D. Caldwell, L. Lindsay, V. Giannini, I. Vurgaftman, T. L. Reinecke, S. A. Maier, and O. J. Glembocki, Low-loss, infrared and terahertz nanophotonics using surface phonon polaritons, Nanophotonics **4**, 44 (2015).

[40] A. Sakurai, K. Yada, T. Simomura, S. Ju, M. Kashiwagi, H. Okada, T. Nagao, K. Tsuda, and J. Shiomi, Ultranarrow-band wavelength-selective thermal emission with aperiodic multilayered metamaterials designed by bayesian optimization, ACS Central Sci. **5**, 319 (2019).

[41] E. Ashalley, K. Acheampong, L. V. Besteiro, P. Yu, A. Neogi, A. O. Govorov, and Z. M. Wang, Multitask deep-learning-based design of chiral plasmonic metamaterials, Photon. Res. **8**, 1213 (2020).

[42] C. Yang, S. Niu, H. Chang, Y. Wang, Y. Feng, Y. Zhang, G. Li, S. Chen, Y. Qu, and L. Xiao, Thermal infrared and broadband microwave stealth glass windows based on multi-band optimization, Opt. Express **29**, 13610 (2021).

[43] D. C. Tzarouchis and A. Sihvola, Polarizability of radially inhomogeneous subwavelength spheres, Phys. Rev. Appl. **10**, 054012 (2018).

[44] D. Navajas, J. M. Pérez-Escudero, M. E. Martínez-Hernández, J. Goicoechea, and I. Liberal, Addressing the impact of surface roughness on epsilon-near-zero silicon carbide substrates, ACS Photon. **10**, 3105 (2023).

[45] www.miracle-concrete.eu.